ACS Photonics

pubs.acs.org/journal/apchd5

Article

Super-Resolution Orthogonal Deterministic Imaging Technique for Terahertz Subwavelength Microscopy

Hichem Guerboukha, Yang Cao, Kathirvel Nallappan, and Maksim Skorobogatiy*

Cite This: *ACS Photonics* 2020, 7, 1866−1875

Read Online

ACCESS | Metrics & More | Article Recommendations | Supporting Information

ABSTRACT: Terahertz subwavelength imaging aims at developing THz microscopes able to resolve deeply subwavelength features. To beat the diffraction limit, the current trend is to use various subwavelength probes to convert the near-field to the far-field. These techniques offer significant gains in spatial resolution but suffer from low light throughput and are slow due to the necessity of a slow pixel-by-pixel raster scan. In parallel, in the visible spectral range, super-resolution imaging techniques enhance the image resolution by statistically correlating multiple frames of an object backlit by stochastically blinking fluorophores. In this work, we develop a super-resolution imaging technique for the THz range, that we name super-resolution orthogonal deterministic imaging (SODI). Since there are no natural THz fluorophores, we design artificial fluorophores in the form of optimal mask sets brought close to the object. By deterministically controlling the blinking, we avoid statistical averages and reconstruct high resolution images using very few frames. After developing the theoretical basis of SODI, we experimentally demonstrate the second-order resolution improvement using only eight phase and binary amplitude masks. We then show how to extend the SODI technique to higher orders to further improve the resolution. Our methodology can be readily adapted with existing THz phase-sensitive single-pixel imaging systems or any THz amplitude imaging arrays. Finally, this work can be of interest to the optical community in other wavelengths, as our technique can be used to deterministically structure light at a subwavelength scale in order to improve the image resolution with few frames and achieve real-time super-resolution microscopy.

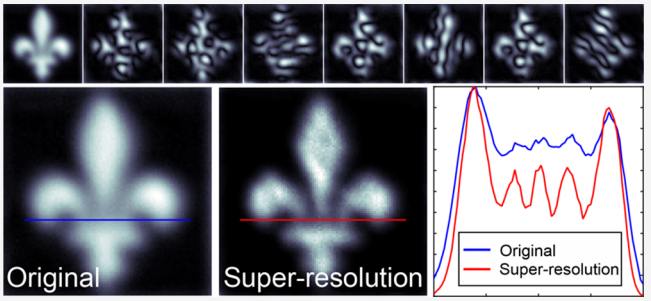

KEYWORDS: *terahertz, imaging, super-resolution, near-field microscopy, computational imaging*

Terahertz science and technology (0.1−10 THz, wavelengths of 3 mm to 30 μm) are now mature research fields with many fundamental and practical applications in sensing and imaging.[1,2] THz subwavelength imaging, in particular, aims at developing THz microscopes able to resolve deeply subwavelength features.[3] To improve the spatial resolution beyond the diffraction limit, a current trend in the THz research is to use various subwavelength probes, such as apertures,[4] metallic tips,[5] solid immersion lenses,[6] dielectric cuboids,[7] and so on that essentially facilitate the creation and scattering of an evanescent subwavelength-sized near-field probing wave into the far-field. While these techniques offer significant gains in spatial resolution, they inherently lack the ability to rapidly obtain THz images due to the necessity of slow pixel-by-pixel raster scans and often long averaging times caused by low measured signal intensities.

To overcome these challenges, several designs of subwavelength imaging systems have been proposed, where the sample is in direct contact with a multipixel detector for parallel pixel acquisition. In one of these approaches, the sample is brought in contact with a nonlinear crystal, which is then used for two-dimensional electro-optic sampling with a sensitive visible CCD camera.[8,9] Recently, a fully integrated THz near-field camera was developed where both the emitter and the detector were fabricated on the same chip using a SiGe heterojunction bipolar transistor technology.[10] While promising, these techniques require direct physical contact between the sample and the detector, which is practically inconvenient.

Computational imaging techniques have also been developed for applications in the terahertz range, including single-pixel imaging and compressive sensing.[11] There, a semiconductor substrate is used as a spatial light modulator when optically pumped.[12] Specially designed patterns obtained using a digital micromirror device are then used as illumination masks for imaging with single-pixel detectors. Moreover, subwavelength imaging can be achieved by placing the sample in direct contact with the mask, allowing to encode near-field features in the reconstructed image.[13,14]

Received: April 29, 2020
Published: June 18, 2020

https://dx.doi.org/10.1021/acsphotonics.0c00711
ACS Photonics 2020, 7, 1866−1875

In parallel, in the visible spectral range, several practically important super-resolution imaging techniques have been developed to beat the diffraction limit.[15,16] These techniques use temporally uncorrelated blinking fluorophores distributed spatially as subwavelength probes, and they involve a computational treatment of a collection of images (frames) that represent snapshots of the target object backlit by randomly blinking fluorophores. One of such techniques is known as super-resolution optical fluctuation imaging (SOFI).[17,18] By assuming that the fluorescent labels switch rapidly and stochastically between binary on/off states, a higher-resolution image is reconstructed from a collection of frames, using the statistics of cumulants. The key advantage of this technique is that one forgoes the slow raster scanning with subwavelength probes or image acquisition in the object near-field while only collecting intensity images in the far-field. This allows realizing super-resolution imaging using only far-field acquisitions with amplitude-sensitive detector arrays (that are now also available in the THz range[19,20]), which is both practical and convenient in most industrial settings.

For these reasons, we explore in this paper the possibility of adopting the SOFI technique to the THz spectral range. An immediate problem that we face is the lack of natural fluorophores in the THz range, with the exception of some exotic atomic optical fluorescence.[21] Nonetheless, since the THz wavelengths are relatively large, we propose to use optimal ensembles of "artificial blinking fluorophores" in the form of judiciously designed amplitude or phase masks brought in close proximity with the object. While in this paper we fabricate both amplitude and phase masks using etching and 3D printing techniques, amplitude masks can also be realized dynamically via spatial light modulation, as used in THz single-pixel imaging and compressive sensing.[13] Importantly, since we directly control the form of the masks, rather than relying on statistical averages of a large number of frames, as it is done in SOFI, we rather aim at employing the smallest possible number of optimally designed super-resolution masks to reduce the number of frames necessary to deterministically reconstruct the image. This is important, because limited frame acquisition rate is one of the key challenges of the SOFI technique even in the visible spectral range.

We also note that the proposed technique which we refer to as Super-resolution Orthogonal Deterministic Imaging (SODI), while superficially similar to compressive sensing, is different from it conceptually and experimentally. Thus, in compressive imaging one generates a number of masks that are typically a fraction of the desired number of pixels,[22,23] leading to loss of information during the image reconstruction. A single-pixel detector can be used within compressive sensing technique. In contrast, within SODI, one uses the smallest possible number of subwavelength-structured "orthogonal" masks necessary for deterministic image reconstruction up to any desired resolution order. Within SODI, a higher order of the reconstruction means subwavelength resolution proportional to the wavelength divided by the square root of the order number, while the super-resolved imaging is reconstructed without loss of information. Additionally, within SODI, amplitude-sensitive (pyroelectric, bolometer, etc.) or phase-sensitive (EOS/CCD) detector arrays can be used in the far-field.

On the other hand, SODI employs an ensemble of masks with subwavelength features and, in this respect, it bears resemblance to techniques that employ near-field to far-field conversion using subwavelength probes. That said, individual masks in SODI show high light throughput (100% phase masks and 50% amplitude masks), which is significantly higher compared to other standard subwavelength probes such as apertures and needles. Additionally, raster scanning of the object with a subwavelength probe is replaced by consecutive image acquisitions in the far-field using an ensemble of optimally designed masks that cover the whole image.

The paper is organized as follows. First, we present a theoretical foundation behind the SODI technique and detail the design of optimal ensembles of amplitude and phase masks that mimic sets of stochastically blinking fluorophores. Then, we present an example of phase masks and demonstrate experimental super-resolution imaging at the second order. Next, we show how to modify the super-resolution algorithm to be able to use binary amplitude (on/off) masks and again demonstrate super-resolution imaging at the second order. We then demonstrate how to improve the resolution further, by providing algorithms for amplitude and phase mask design for higher order super-resolution imaging. Finally, we discuss on how the SODI algorithm can be used in existing THz imaging modalities to increase their current resolutions.

SUPER-RESOLUTION RECONSTRUCTION USING DETERMINISTIC FLUCTUATIONS, SECOND ORDER FORMULATION

The following presentation is largely based on the mathematical foundation behind the SOFI technique.[17,18] Considering a linear imaging system, the measured image $E(\vec{r})$ is the spatial convolution of the object $O(\vec{r})$ with the system's impulse response $S(\vec{r})$, also known as the point spread function (PSF):

$$E(\vec{r}) = \int \mathrm{d}\vec{r}_1 S(\vec{r} - \vec{r}_1)\cdot O(\vec{r}_1)M(\vec{r}_1, t) \tag{1}$$

Within the SOFI technique $M(\vec{r},t)$ in eq 1 corresponds to the time-dependent spatial distribution of light intensity emitted by deeply subwavelength stochastically blinking fluorophores. In our SODI adaptation of this technique, $M(\vec{r},t)$ corresponds to the complex transmission function of a given subwavelength-structured mask labeled with index $t \in [1,N_t]$, where N_t is the number of masks in a measurement set (also equal to the number of images to be acquired during the experiment). We start by considering the variance of the image. By denoting $\langle\cdots\rangle_t$ to be a simple average over a collection of frames, we obtain

$$\langle E^2(\vec{r}, t)\rangle_t - \langle E(\vec{r}, t)\rangle_t^2 = \iint \mathrm{d}\vec{r}_1\mathrm{d}\vec{r}_2 S(\vec{r} - \vec{r}_1)S(\vec{r} - \vec{r}_2)O(\vec{r}_1)O(\vec{r}_2) \times (\langle M(\vec{r}_1, t)M(\vec{r}_2, t)\rangle_t - \langle M(\vec{r}_1, t)\rangle_t\langle M(\vec{r}_2, t)\rangle_t) \tag{2}$$

In general, taking the square of the image does not result in a higher-resolution image. It is a somewhat subtle point as, for example, a squared grayscale image will appear to have sharper/narrower boundaries; however, if two lines in such an image appear as one, the same will be observed in the squared image. To get higher resolution within the SOFI technique one assumes that any two fluorophores blink independently. Then, one can define the following averaging function over a time period Δt and the corresponding orthogonality relation between light intensities emitted by the two point-size fluorophores:

https://dx.doi.org/10.1021/acsphotonics.0c00711
ACS Photonics 2020, 7, 1866−1875

$$\langle M(\vec{r}_1, t)M(\vec{r}_2, t)\rangle_t - \langle M(\vec{r}_1, t)\rangle_t\langle M(\vec{r}_2, t)\rangle_t$$
$$= \frac{1}{\Delta t}\int_0^{\Delta t} dtM(\vec{r}_1, t)M(\vec{r}_2, t) - \left(\frac{1}{\Delta t}\int_0^{\Delta t} dtM(\vec{r}_1, t)\right)$$
$$\left(\frac{1}{\Delta t}\int_0^{\Delta t} dtM(\vec{r}_2, t)\right)$$
$$= C\cdot\delta(\vec{r}_1 - \vec{r}_2) \quad (3)$$

where C is assumed to be a spatially independent constant and $\delta(\vec{r})$ is the delta function. With this orthogonality relation, the reconstructed image (eq 2) becomes

$$\langle E^2(\vec{r}, t)\rangle_t - \langle E(\vec{r}, t)\rangle_t^2$$
$$= \frac{1}{\Delta t}\int_0^{\Delta t} dtE^2(\vec{r}, t) - \left(\frac{1}{\Delta t}\int_0^{\Delta t} dtE(\vec{r}, t)\right)^2$$
$$= C\cdot\int d\vec{r}_1 S^2(\vec{r} - \vec{r}_1)O^2(\vec{r}_1) \quad (4)$$

Since a PSF squared is narrower than the original PSF, one will observe improvement in the image resolution. For example, frequently, the PSF can be expressed as a Gaussian of width σ:

$$S(\vec{r}) = \exp\left(-\frac{|\vec{r}|^2}{2\sigma^2}\right) \quad (5)$$

Therefore, taking the square of that Gaussian yields another Gaussian of a reduced width $\tilde{\sigma} = \sigma/\sqrt{2}$, thereby leading to an improved resolution.

Similarly, within SODI, by judiciously designing a set of mutually orthogonal masks and by properly choosing the frame averaging operator $\langle\cdots\rangle_t$, we can obtain a higher-resolution image reconstruction as will be demonstrated in the rest of this section. In the following, we detail several design principles for the construction of the optimal mask sets $M(\vec{r},t)$ for SODI technique. First, we assume that the PSF has a bounded support:

$$S(\vec{r} - \vec{r}_1)S(\vec{r} - \vec{r}_2) = 0 \quad \text{if} \quad |\vec{r}_1 - \vec{r}_2| > D \quad (6)$$

where D is the characteristic width of the PSF, which is typically set by diffraction on the imaging optics and, thus, $D \propto \lambda$. This also means that two features will be automatically resolved if they are well separated in space by at least a distance D or further (see the example of two Gaussian-like PSFs in Figure 1a). In the case of the SOFI technique, it also means that, to achieve resolution enhancement, one must require that the emission from closely placed point-size fluorophores within a distance D or closer to each other are uncorrelated. At the same time, fluorophores that are positioned further than D from each other will not affect resolution, even if they blink in a correlated manner. In the case of the SODI technique, this means that the mask orthogonality should only be forced locally, within any spatial domain of characteristic size D, while the same mask set does not have to be orthogonal over longer distances:

$$\langle M(\vec{r}_1, t)M(\vec{r}_2, t)\rangle_t = \begin{cases} 0 & \text{if} \quad |\vec{r}_1 - \vec{r}_2| < D \\ C & \text{if} \quad \vec{r}_1 = \vec{r}_2 \end{cases} \quad (7)$$

This realization leads to a significant reduction in the number of required masks/frames to enable resolution enhancement. Thus, a locally orthogonal mask set can be constructed using a basic pixel group and then be periodically repeated to cover the whole object under imaging. According to eq 7, the physical size of the basic pixel group must be comparable to the PSF size. Furthermore, we are not limited to using square tiling of the basic pixel groups, as triangular or hexagonal tiling can also be used to cover the two-dimensional plane (Figure 1b).

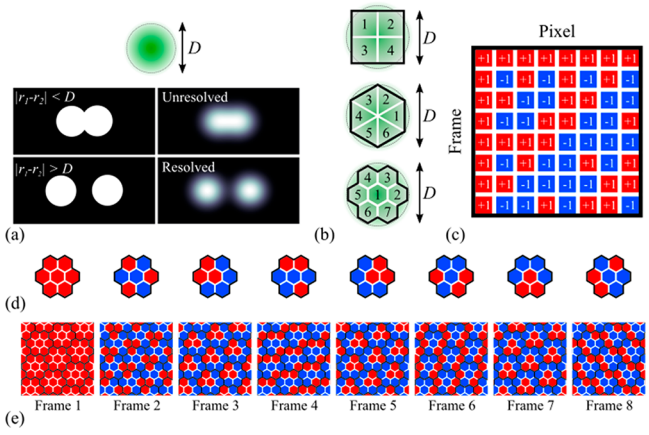

Figure 1. Super-resolution image reconstruction with deterministic fluctuations. (a) Two features are resolved if they are separated in space further away than the characteristic size D of the PSF spread function. (b) Examples of basic pixel groups containing four square pixels, six triangular pixels, and seven hexagonal pixels for periodic tiling of the 2D plane. (c) Hadamard matrix used in the second-order reconstruction. Here, different matrix rows define pixel values in the basic pixel groups of different masks. (d) Basic pixel groups of the eight masks based on the Hadamard basis and (e) corresponding eight complete masks, where the basic pixel groups are periodically tiled to cover the whole field-of-view.

Note that the orthogonality definition given by eq 7 is somewhat different from that used in eq 3. As we will see in the following, we used eq 7 for pure phase masks, while eq 3 was used later in the paper for amplitude masks.

Next, we consider digital masks that feature a small number of pixels in the basic pixel group. This means that pixel positions in the mask can accept a finite and discrete number of values N_r, and we label individual pixels with an index r (see Figure 1b). Then, the local orthogonality condition for the digital masks (assuming periodic tiling of the basic pixel group to cover the whole plane) can be, for example, expressed as

$$\langle M(\vec{r}_1, t)M(\vec{r}_2, t)\rangle_t = \frac{1}{N_t}\sum_{t=1}^{N_t} M(r_1, t)M(r_2, t)$$
$$= \begin{cases} C & \text{if} \quad r_1 = r_2 \\ 0 & \text{if} \quad r_1 \neq r_2 \end{cases}; \; r_1, r_2 \in [1, N_r] \quad (8)$$

where N_t is the total number of masks, t is the mask number, while r_1,r_2 is the pixel numbers within the basic pixel group, and C is a common constant that is independent of pixel position. As we show later, we used the mask orthogonality condition defined in eq 8 to design pure phase masks. Using a mask set that satisfies eq 8, one must acquire N_t far-field images $E(\vec{r},t)$ of the object covered by the different masks in this set. Then, an image of the object with increased resolution can be reconstructed using

$$\langle E^2(\vec{r}, t)\rangle_t = \frac{1}{N_t}\sum_{t=1}^{N_t} E^2(\vec{r}, t) = C\int d\vec{r}_1 S^2(\vec{r} - \vec{r}_1)O^2(\vec{r}_1) \quad (9)$$

As in the SOFI technique, the resolution is improved because the PSF is squared in eq 9. The mask set can be better

https://dx.doi.org/10.1021/acsphotonics.0c00711
ACS Photonics 2020, 7, 1866−1875

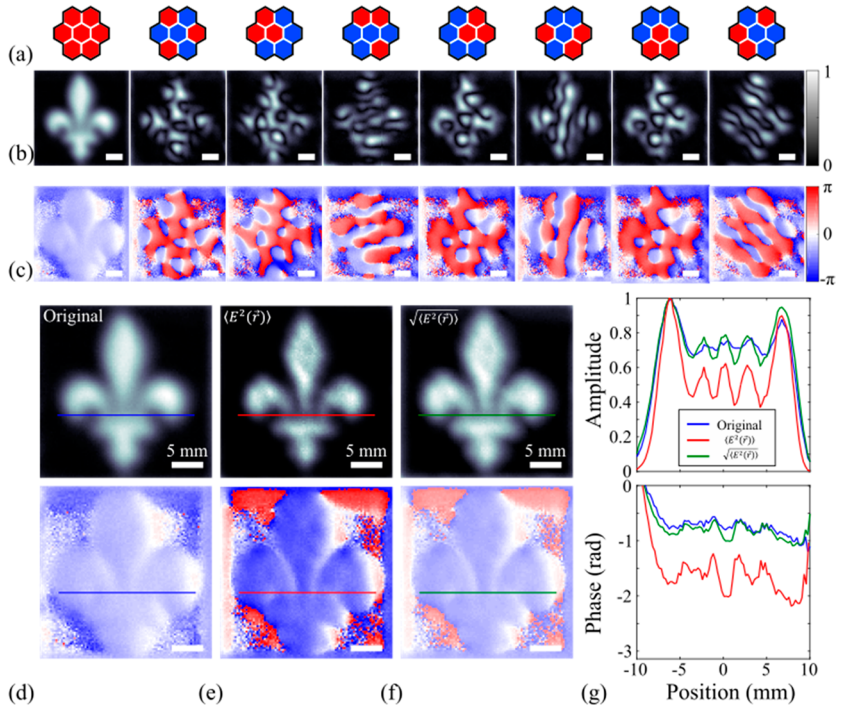

Figure 2. Second order image reconstruction using phase masks based on the Hadamard basis. (a) Basic pixel groups of each mask. (b) Amplitude and (c) phase of the corresponding measured frames. (d) Amplitude (top) and phase (bottom) of the original image, (e) the super-resolution reconstruction using $\langle E^2 \rangle$ and (f) $\sqrt{\langle E^2 \rangle}$ images. (g) Linear section of the amplitude (top) and phase (bottom) distributions along the line where the three leaves meet. Scale bar size is 5 mm.

visualized using a matrix notation, where the matrix rows correspond to the individual masks, the columns correspond to the individual pixels in the basic pixel group, while the matrix values are the corresponding $M(r,t)$. For example, a locally orthogonal set containing $N_t = 2^k$ pure phase masks can be constructed using Hadamard matrix (Figure 1c), where the columns are all mutually orthogonal vectors in the sense of eq 8. At the same time, we are not forced to use all the columns of the Hadamard matrix to form a locally orthogonal set of masks, so in fact, the number of pixels N_r in the basic pixel group can be smaller than the number of masks N_t. At the same time, using periodic tiling of the basic pixel set ensures that no matter what pixel is chosen in the object plane, a thus designed mask set will always be locally orthogonal in the sense of eq 8. As an example, in Figure 1b, we show three different choices of basic pixel groups that contain $N_r = 4$, 6, and 7 pixels that can be tiled periodically to fill the 2D plane. Then using the Hadamard matrix (Figure 1c), one can construct locally orthogonal sets of $N_t = 8$ phase masks (with either 0 or π phase shifts) containing N_r pixels in the corresponding basic pixel group (Figure 1d). By tiling the basic pixel groups periodically to fill the whole 2D plane, one arrives at a complete set of locally orthogonal masks shown in Figure 1e. Finally, in order to ensure that all pixels in a basic pixel set contribute equally to the image reconstruction, we require that the constant C in eq 8 is the same for all the pixels in a given mask set. In other words, this ensures that, on average, the object is uniformly illuminated by the masks.

PURE PHASE MASKS

In Figure 2 we present experimental results of the SODI image reconstruction measured using a THz time-domain imaging system (see Supporting Information, A, for more details about the experimental setup). As described in the previous section, we used Hadamard basis (+1, −1) phase masks where the +1 and −1 elements were, respectively, obtained using phases of 0 and π (through the phase term $\exp(i\phi)$). As an object, we use a cutout in metal in the form of the fleur-de-lis (see Supporting Information, B). As explained above, the eight frames are formed using seven pixels derived from the Hadamard basis arranged in a hexagonal lattice with an interpixel distance of 2 mm (Figure 2a). Knife-edge measurements revealed that the PSF could be expressed as a Gaussian (eq 5) with a width $\sigma(\lambda) = \lambda F\sqrt{2}/\pi D$, in accordance to the Gaussian beam theory (see Supporting Information, C, for details). As shown in Figure S3, the use of an interpixel distance of 2 mm ensured that 99% of the Gaussian PSF could fit in a circle of radius 3σ surrounding the group of pixels. To realize the −1 element of the Hadamard basis, we use phase elements fabricated by 3D printing hexagonal steps of height h using PLA plastic of refractive index $n \approx 1.6$. The incurred phase due to passage through a step of thickness h is $\phi = 2\pi(n-1)h/\lambda$, which indicates that, to obtain a phase difference of π at 0.32 THz ($\lambda \approx 0.94$ mm), we must use $h = 800$ μm. In Figure S2b of the Supporting Information, B, we show eight phase masks that correspond to eight rows of the Hadamard basis/matrix.

We then use THz time-domain spectroscopy for both amplitude and phase super-resolution image reconstruction. In this system, broadband THz pulses are generated and detected by photoconductive antennas to obtain both amplitude and phase images at several frequencies. In particular, for every mask in the 8 mask set, we place the given phase mask on top of the object and then image the pair using raster scanning in the focal plane between two parabolic mirrors (see Supporting Information, A, and Figure S1 for more details). In Figure 2b, we show amplitude images of the resulting interference

https://dx.doi.org/10.1021/acsphotonics.0c00711
ACS Photonics 2020, 7, 1866−1875

patterns, while in Figure 2c the corresponding phase distributions are presented. Next, following eq 9, we compute the super-resolved image by taking the average of the squares of the complex fields from each measurement $\langle E^2(\vec{r},t)\rangle$. We note that we average the complex fields squared and not the intensities, which allows us to retrieve super-resolved images of both amplitude and phase distributions. The original image amplitude and phase are shown in Figure 2d, while our SODI images are shown in Figure 2e,f, where we present both $\langle E^2(\vec{r},t)\rangle$, and $\sqrt{\langle E^2(\vec{r},t)\rangle}$ distributions. We note that $\sqrt{\langle E^2(\vec{r},t)\rangle}$ preserves the same intensity contrast as the original image, while providing better resolution than the original image. Finally, to better see the effect of our algorithm on the resolution, we plot the amplitude and phase cross sections along a line in the image where the three leaves meet. In the original image, the three leaves can hardly be distinguished, while in the super-resolved amplitude and phase images, they are clearly resolvable.

BINARY AMPLITUDE MASKS

In the previous section, we detailed second order SODI technique using a set of pure phase masks based on Hadamard orthogonal basis. In this section, we detail an alternate second-order SODI reconstruction that uses binary amplitude masks that are also related to the Hadamard basis. The case of binary amplitude masks is important as it can be efficiently realized using THz amplitude spatial light modulators based on dynamic photomodulated masks.[12−14]

We now demonstrate how starting from the Hadamard basis that contains +1 and −1 elements (Figure 1c), we can modify the SODI technique and derive an orthogonal set of amplitude masks that contains only 0 and 1 elements and features ∼50% light transmission through each mask. The 0 and 1 elements can be interpreted as opaque and transparent regions of a binary amplitude mask, and they can be realized experimentally as cutouts in an otherwise nontransparent metal foil. Particularly, one can show that by simply replacing the −1 elements by 0 in the Hadamard basis of size N_t and after omitting the first column of 1's, we arrive at a set of N_t binary amplitude masks $\langle M(\vec{r}_1, t)$ each containing $N_r = N_t - 1$ pixels that are locally orthogonal in the following sense:

$$\begin{aligned}&\langle M(\vec{r}_1, t)M(\vec{r}_2, t)\rangle_t - \langle M(\vec{r}_1, t)_t M(\vec{r}_2, t)\rangle_t \\ &= \frac{1}{N_t}\sum_{t=1}^{N_t} M(r_1, t)M(r_2, t) - \frac{1}{N_t}\sum_{t=1}^{N_t} M(r_1, t)\frac{1}{N_t}\sum_{t=1}^{N_t} M(r_2, t) \\ &= \begin{cases} C & \text{if} \quad r_1 = r_2 \\ 0 & \text{if} \quad r_1 \neq r_2 \end{cases}; \; r_1, r_2 \in [1, N_r] \end{aligned} \tag{10}$$

where the constant $C = 3/4$ for the binary amplitude mask set derived from the Hadamard basis of any order N_t.

The SODI technique modified for amplitude mask sets then requires a subtraction of the squared mean of the measured electric field from the mean of the square of the electric field, where averaging is performed over the set of N_t amplitude masks:

$$\begin{aligned}&\langle E^2(\vec{r}, t)\rangle_t - \langle E(\vec{r}, t)\rangle_t^2 \\ &= \iint d\vec{r}_1 d\vec{r}_2 S(\vec{r} - \vec{r}_1)S(\vec{r} - \vec{r}_2)O(\vec{r}_1)O(\vec{r}_2)[\langle M(\vec{r}_1, t)M(\vec{r}_2, t)\rangle \\ &\quad - \langle M(\vec{r}_1, t)\rangle \times \langle M(\vec{r}_2, t)\rangle] \\ &= C\iint d\vec{r}_1 S^2(\vec{r} - \vec{r}_1)O^2(\vec{r}_1) \end{aligned} \tag{11}$$

It is important to mention that the orthogonality condition at eq 10 is different from the usual orthogonality condition used for the phase masks (eq 8). In addition to be compatible with binary amplitude masks, the case described in this section indicates that there is no restriction in the definition of the super-resolution algorithm. In principle, one can use any function of the measured frames as long as the corresponding orthogonality is respected with the appropriate mask set. Moreover, the choice we made here is not unique for binary amplitude masks. For example, one could use the usual orthogonality condition (eq 8) and measure two sets of Hadamard matrices (one positive, where −1s are transformed to 0s and one negative where 1s are transformed to 0s). Then, the two sets should be subtracted before applying the SODI algorithm (eq 9).[12] Compared to the solution presented in this section (eq 10), this technique would have essentially doubled the number of measurements, as one would need to measure the positive Hadamard mask set separately from the negative one.

In Figure 3, we present experimental results of the SODI reconstruction using binary amplitude masks derived from the

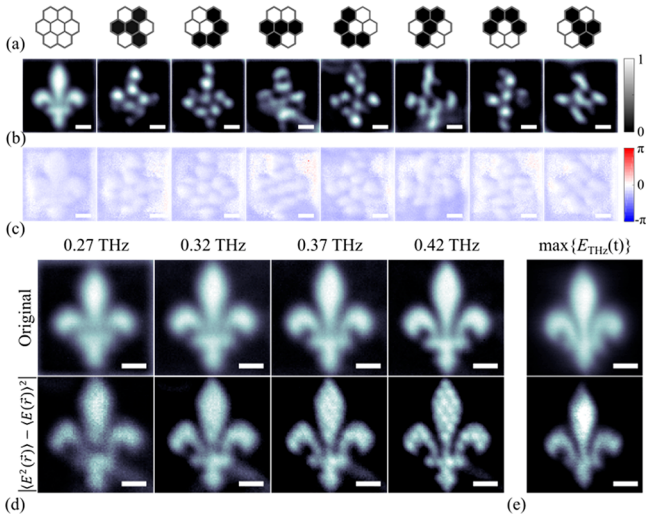

Figure 3. Second order image reconstruction using binary amplitude masks constructed using a modified Hadamard basis. (a) Basic pixel groups in each mask. (b) Amplitude and (c) phase of the corresponding measured frames. (d) Comparison of the amplitude of the original images (top) and their corresponding super-resolution reconstructions using complex electric field (bottom) at different frequencies and (e) when considering only the maximum electric field peak value in time domain. The super-resolution reconstructions of the phase are shown in Supporting Information, D. Scale bar size is 5 mm.

Hadamard basis (Figure 3a). Measured at 0.32 THz amplitude and phase distributions for a fleur-de-lis image superimposed with different masks are shown in Figure 3b and c, respectively. The amplitude of the original image and its corresponding super-resolution reconstruction are shown in Figure 3d at various frequencies from 0.27 to 0.42 THz. The SODI images

https://dx.doi.org/10.1021/acsphotonics.0c00711
ACS Photonics 2020, 7, 1866−1875

for the reconstructed phases are shown in Supporting Information, D. Unlike the phase masks, which are designed to operate at a specific THz frequency (since the phase of the underlying phase element is frequency dependent), the SODI reconstruction using amplitude mask sets can be performed over a larger bandwidth. However, when increasing the THz frequency, we start observing artifacts in the reconstruction image in the form of multiple dots (high spatial frequency noise). These appear because the PSF size at higher frequencies becomes smaller than the size of the basic pixel group of the patterned mask; therefore, the local orthogonality condition between blinking patterns of the individual pixels, eq 10, might not hold anymore due to partial overlap of the PSF spatial support with the individual pixels. To study in more details the observed numerical artifacts, we performed additional numerical simulations that are presented in Supporting Information, E.

Finally, although in our experiments we used a THz-TDS imaging system and were, therefore, capable of super-resolving both amplitude and phase distributions, the SODI technique is not restricted to coherent measurements and it can be performed using field intensities instead of electric fields. Indeed, our super-resolution algorithm does not specify the nature of the frames $E(\vec{r},t)$. As long as the image can be represented as the convolution of some measurand with a given PSF (eq 1), the SODI algorithm can be applied. For example, in Figure 3e, we show SODI reconstruction using the maximum amplitude value of the peak THz electric field in time domain. This measurand is often used to reconstruct THz images, as it provides rapid images without the need to move the optical delay line of the THz-TDS system.[14] Again, we observe the resolution improvement using only the peak THz electric field.

In the previous sections, we showed two ways to perform the SODI reconstruction using phase and binary amplitude masks. In general, phase masks are preferable since they allow a complete transmission of light while binary amplitude masks block a portion of it. However, the choice of either using amplitude or phase masks is mostly determined by the practical ability to easily create and shuffle such masks. We discuss more in detail the available options later.

SUPER-RESOLUTION RECONSTRUCTION USING DETERMINISTIC FLUCTUATIONS, HIGHER ORDER FORMULATION

In the previous sections, we have detailed the second order SODI algorithm for image resolution enhancement. Naturally, one can construct higher order super-resolution schemes by using higher moments in the definition of the algorithm. In the following, we present one possible formulation that is most applicable to the case of phase masks. Particularly, for the *n*th-order algorithm, one needs to calculate:

$$\begin{aligned}&\langle E^n(\vec{r},t)\rangle_t\\&=\iint \mathrm{d}\vec{r}_1\mathrm{d}\vec{r}_2\ldots\vec{r}_n\cdot S(\vec{r}-\vec{r}_1)S(\vec{r}-\vec{r}_2)\ldots S(\vec{r}-\vec{r}_n)O(\vec{r}_1)O(\vec{r}_2)\\&\quad\ldots O(\vec{r}_n)\langle M(\vec{r}_1,t)M(\vec{r}_2,t)\ldots M(r_n,t)\rangle_t\end{aligned}\tag{12}$$

The local orthogonality condition for a given mask set can be defined as

$$\begin{aligned}&\langle M(\vec{r}_1,t)M(\vec{r}_2,t)\ldots M(\vec{r}_n,t)\rangle_t\\&=\frac{1}{N_t}\sum_{t=1}^{N_t}M(\vec{r}_1,t)M(\vec{r}_2,t)\ldots M(\vec{r}_n,t)\\&=\begin{cases}C & \text{if } \vec{r}_1=\vec{r}_2=\ldots\vec{r}_n\\0 & \text{else}\end{cases}\end{aligned}\tag{13}$$

where $M(\vec{r},t)$ is considered a vector of size N_t with elements that describe changing optical properties over time of a fixed pixel/fluorophore located at position $\vec{r}$. Then, the reconstructed image is convoluted with the n^{th} power of the PSF:

$$\langle E^n(\vec{r},t)\rangle_t=\iint \mathrm{d}\vec{r}_1 S^n(\vec{r}-\vec{r}_1)O^n(\vec{r}_1)\tag{14}$$

As previously, considering a Gaussian PSF of width σ (eq 5), taking it to the n^{th} power results in another Gaussian with a reduced width $\tilde{\sigma}=\sigma/\sqrt{n}$, thus, leading to an improved resolution.

Finding a basis that respects the orthogonality condition eq 14 for a general order *n* is not trivial. An obvious choice for any order *n* is the identity matrix, the columns of which form "blinking" patterns $M(\vec{r},t)$ of artificial fluorophores. This choice, however, results in binary amplitude masks with very low transmission efficiency, as only one pixel in the basic pixel group is 1 (transmitting), while all the other pixels are 0 (blocking the light). This resulting mask set corresponds to a subwavelength aperture successively scanning the object pixel by pixel. Moreover, following Bethe's study of diffraction by a circular hole,[24,25] the transmitted electric field decreases with the third power of the aperture size, thus, significantly decreasing the overall signal-to-noise ratio of the measurements. In contrast, light transmission through pure phase masks is significantly more efficient, as was demonstrated in Pure Phase Masks when using, for example, a Hadamard basis. Therefore, when increasing the order of the SODI method, one is interested in using mask sets with high light transmission. Additionally, for convenience of the mask fabrication, we seek to use either pure phase or binary amplitude masks.

It is important to mention that the mask orthogonality condition defined by eq 13 is not the traditional definition of an orthogonal basis set, which requires that the scalar product between any two distinct vectors in a set is zero. In fact, for the SODI method of order *n*, an orthogonal basis set in the sense of eq 13 requires that the convolution of any *n* vectors in a set, among which at least two are different to be equal to zero. To the best of our knowledge, the problem of finding orthogonal basis for higher order orthogonality definition in this sense is still an open problem that does not have a general solution. Finally, we note that higher order super-resolution reconstruction formulations that are alternative to eq 12 can be formulated as one only needs a certain general orthogonality condition between the individual blinking patterns of spatially distinct pixels, while the main advantage of eq 12 is its simplicity.

In what follows, we present some particular solutions that we found for the problem of high-order orthogonal basis sets in the sense of eq 13. We first present a solution for the third order orthogonal basis set containing any desired number of N_r vectors (number of pixels in the basis pixel group). An example of a fourth-order orthogonal basis set can be found in Supporting Information, F. As discussed earlier, temporal

https://dx.doi.org/10.1021/acsphotonics.0c00711
ACS Photonics 2020, 7, 1866−1875

changes in the optical properties of a fluorophore (artificial blinker) located at position $\vec{r}$ are described by the function $M(\vec{r},t)$. By limiting ourselves to a finite group of N_r pixels in the basic pixel group and considering only N_t temporal snapshots (number of masks), we adopt a matrix notation where M is a rectangular matrix of dimensions $N_t \times N_r$, where the rows correspond to the different time frames, while the columns correspond to the different pixels. Consider now n columns of the matrix M with column indices r_1, r_2, ..., r_n. The orthogonality relation of the n^{th}-order (eq 13) can then be written as

$$\begin{aligned}&\langle M(r_1, t)M(r_2, t)...M(r_n, t)\rangle_t \\ &= \frac{1}{N_t}\sum_{t=1}^{N_t} M(r_1, t)M(r_2, t)...M(r_n, t) \\ &= \begin{cases} C & \text{if } r_1 = r_2 = ... = r_n \\ 0 & \text{else} \end{cases}; \; r_1, r_2, ..., r_n \in [1, N_r] \end{aligned} \tag{15}$$

To verify the n^{th} order orthogonality condition of eq 15 for a given matrix of size $N_t \times N_r$, one should compute the N_r^n possible combinations of vector multiplications to ensure that it is always equal to 0, except when all the indices are equal. In fact, due to the commutative property of the product defined in eq 15, the number of distinct multiplications is significantly smaller and can be shown to be equal to $\frac{(n+N_r-1)!}{n!\,(N_r-1)!} \sim \frac{N_r^n}{n!}$.

For the third order orthogonality condition, we found a pure phase basis set for any number of pixels N_r. The matrix with columns made of basis vectors is constructed by concatenation of the three following matrices. By denoting I_N to be the identity matrix of size N and by denoting $O_{N\times M}$ to be the matrix of size $N \times M$ with every element equal to one, the three matrices can be written as

$$\begin{aligned} A_1 &= O_{N_r\times N_r} - (1 - i)I_{N_r} \\ A_2 &= O_{N_r\times N_r} - (1 + i)I_{N_r} \\ A_3 &= -O_{2(N_r-3)\times N_r} \end{aligned} \tag{16}$$

The matrix of size $(4N_r - 6) \times N_r$ resulting from the concatenation of these three matrices along the temporal dimension forms a third order orthogonal basis in the sense of (eq 15). Compared to the Hadamard basis, this solution contains four different phase elements, $\{+1, +i, -1, -i\}$, that can be obtained using a mask with respective phases $\left\{0, \frac{\pi}{2}, \pi, \frac{3\pi}{2}\right\}$. For example, using the same 3D printed phase mask demonstrated previously (at 0.32 THz), the respective thicknesses would be $\{0, 400, 800, 1200\}$ μm. The number of required frames is a function of the number of pixels: $N_t = 4N_r - 6$. However, one can see that all the pixels in the last $2(N_r - 3)$ frames are constituted of -1 elements. Therefore, one can in principle measure it only once and reuse it $2(N_r - 3)$ times when taking the average. The smallest number of required frames/masks would then be $N_t = 2N_r + 1$.

We show in Figure 4a an example of such a basis made of $N_r = 4$ vectors (number of pixels in the basic pixel group), each containing $N_r = 4$ elements (number of masks in the mask set). To demonstrate that this basis set respects the third order orthogonality condition, we compute the 20 distinct combinations of vectors entering the definition (eq 15), with $n = 3$. As we can see in Figure 4b, the 20 possible

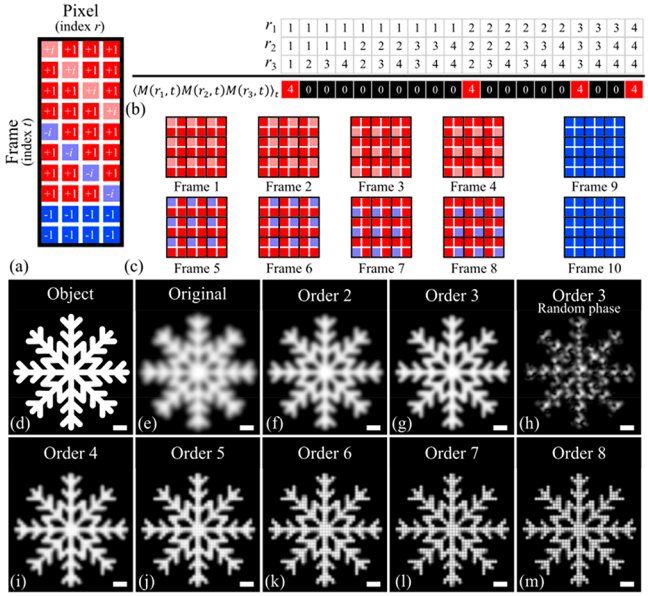

Figure 4. Higher order image reconstruction. (a) Third order orthogonal basis set (see eq 16) with $N_r = 4$ vectors (number of pixels in the basic pixel group). (b) The third order orthogonality relation $\langle M(r_1,t)M(r_2,t)M(r_3,t)\rangle_t = 0$ is observed when at least one of the vectors is different from the others. (c) 10 locally orthogonal phase masks that correspond to the third order orthogonal basis resulting from periodic patterning of the plane with 2×2 square tiles. (d) Object representing a snowflake cutout and (e) original image obtained by convolution with a Gaussian PSF of width $\sigma = 1$ mm. (f–n) Super-resolution reconstruction of different orders: (f) Order 2 with Hadamard basis (16 phase masks); (g) Order 3 following eq 16 (33 phase masks); (h) Order 3 with random phase masks to show the importance of using locally orthogonal mask sets (33 masks); (i) Order 4 with the pure phase basis detailed in Supporting Information, F (256 phase masks); (j) Order 5; (k) Order 6; (l) Order 7; (m) Order 8 with an identity matrix as a basis set (16 binary amplitude masks in the form of a subwavelength aperture). Scale bar size is 5 mm.

multiplications always yield 0, except in the four cases when all the three vectors are identical. We then arrange the four pixels that make the basic pixel group into a 2×2 square tile and repeat it periodically, which results in 10 distinct masks shown in Figure 4c.

In Figure 4e–m, we numerically compare different orders of reconstruction of a 45×45 mm object in the form of a snowflake cutout (Figure 4d). The convolution of the object with a Gaussian PSF of width $\sigma = 1$ mm (as defined in eq 7) is shown in Figure 4e. To apply the SODI algorithm, we consider the basic pixel group of $N_r = 16$ pixels arranged in a 4×4 square tile, with the diagonal equal to 6σ, which comprises 99.7% of the Gaussian PSF. The square tiles are then periodically patterned to cover the whole object. For a given order of the SODI reconstruction algorithm, we then choose an appropriate orthogonal basis set and the corresponding set of masks. We then compute the convolution of the masks with the object and the Gaussian PSF using eq 1. Finally, to obtain higher-resolution images, we compute the n^{th} order SODI reconstruction using [eq 14]. The result for order 2 is obtained with a Hadamard basis of $N_t = N_r = 16$ phase masks (Figure 4f), while the result for order 3 is constructed using the matrix described by eq 16 with $N_t = (2N_r + 1) = 33$ phase masks (Figure 4g). To clearly demonstrate the necessity of using the

https://dx.doi.org/10.1021/acsphotonics.0c00711
ACS Photonics 2020, 7, 1866–1875

orthogonal basis sets for super-resolution image reconstruction, in Figure 4h, we present a third order reconstruction using random phase matrices instead of the orthogonal ones, clearly the resultant reconstruction is incorrect. For order 4 in Figure 4i, we use the fourth order orthogonal phase-only basis set that we detail in the Supporting Information, F, with 256 phase masks. Finally, the results for orders 5 to 8 are obtained using a basis set in the form of an identity matrix that corresponds to successive scanning of the object with a subwavelength aperture of size equal to the size of the single pixel (16 amplitude masks).

As one can see, the resolution of the snowflake improves when increasing the order n. However, there is a limit in the improvement, as seen in Figure 4j–m. Artifacts in the reconstruction in the form of discrete dots start to appear when the size of the single pixel in the basic pixel group becomes larger than the width of the n^{th}-power PSF $\sigma/\sqrt{n}$. To avoid this problem, one could reduce the size of the individual pixels used in the mask definition at the expense of increasing the number of masks/frames necessary for image reconstruction.

Mathematically speaking, in principle, there is no limit in the achievable resolution when increasing the order n and decreasing the size of the subpixels. The reason is that when the individual fluorophores are infinitesimally small, they can be considered as delta functions. Then, the SODI reconstruction integral is exact regardless of the reconstruction order n. Of course, for various physical reasons, this mathematical observation cannot be practically achieved. First, there is a minimal size of the fluorophores. This is, of course, limited by the available physical techniques to realize the masks. Also, by decreasing the size of the fluorophores, one increases the necessary frames for the reconstruction. In the limit when the masks are infinitesimal, the reconstruction time becomes infinite. Moreover, the masks must be extremely close to the object (this is the meaning of the multiplication between the object $O(\vec{r})$ and the masks $M(\vec{r},t)$ in eq 1). In reality, there is always a finite distance between the two that results in diffraction effects and reduced resolution. Finally, our mathematical approach does not include any noise contribution. In practice, these impose a practical limit to the measurable signals.

DISCUSSION

We now comment on the possibility of using the SODI technique with other imaging modalities developed in the THz range. First and foremost, the SODI technique supposes a linear imaging system, i.e. the image can be represented as the convolution of the object with a point spread function (see eq 1). Fortunately, most of THz imaging systems fulfill this requirement. As we discussed earlier, the SODI algorithm improves the resolution of existing imaging systems by a factor of $\sqrt{n}$, where n is the order of the SODI reconstruction. This is achieved by reducing the PSF width to $\tilde{\sigma} = \sigma/\sqrt{n}$. One can define the resolution as the full width at half-maximum (fwhm) of the underlying Gaussian PSF of eq 5. Two points are resolvable if their distance is greater than fwhm $= 2\sqrt{2\ln 2}\sigma$. For example, in our proof of concept, we used a THz time-domain spectroscopy system, and the image was obtained by displacing the object in the focal plane. With our simple diffraction-limited experiment with regular focusing optics (F = 101.6 mm and D = 101.6 mm), we had $\sigma = \lambda\sqrt{2}F/\pi D = \lambda/1.11$ (as confirmed by knife-edge measurements in Supporting Information, C). At 0.32 THz, this corresponded to σ = 0.844 mm and fwhm = 1.9875 mm. Therefore, two features separated by ∼2 mm were initially resolvable (diffraction limit). After performing the SODI algorithm at n = 2 order, the new width was $\tilde{\sigma} = \sigma/\sqrt{n} = \lambda/1.6$, which corresponded to σ = 0.5968 mm and fwhm = 1.4054 mm at 0.32 THz. Therefore, using the SODI algorithm, two features separated by ∼1.4 mm were resolvable, beating the diffraction limit.

In a similar manner, the SODI algorithm can be applied to other THz imaging modalities to improve the resolution. In practice, the SODI technique has two main experimental requirements: the blinking masks and the imaging system itself.

The nature of the masks is an important requirement in the SODI technique. Super-resolution techniques developed in the visible range use fluorophores that blink in an on/off fashion (either light is emitted or not). Under our mathematical framework, this type of blinking is referred to as binary amplitude masks and are constituted of 0 and 1 elements in their matrix representation. In the THz range, as we showed in our experimental demonstration, this type of masks can be fabricated using transparent cutouts in an opaque material (for example, metal). In general, however, the blinking can also occur in the phase. This type of phase blinking can be represented by matrix with complex elements u_i related to the phase $u_i = \exp(j\phi_i)$, as we showed earlier. The choice of either using amplitude or phase masks depends largely on the possibility of easily creating and shuffling such masks. However, phase masks are preferable because they allow higher light throughput, while binary amplitude masks can block a significant portion of it.

Another important requirement is that the masks need to be positioned in the near-field region. In visible SOFI, this requirement is automatically satisfied because the blinking fluorophores are chemically attached to specific molecules in the target object. Therefore, it is important for the artificial blinking fluorophores of the SODI technique to have the same property and be as close as possible to the object. In eq 1, this is the meaning of the direct product between the object $O(\vec{r})$ and the mask function $M(\vec{r},t)$. If the samples are not exactly in the near-field region, eq 1 must be somehow modified to consider the diffraction effect of the masks on the outgoing light, leading to a decrease in the spatial resolution.

In our demonstration, we placed physical masks (3D-printed phase masks and metallic binary masks) in direct contact with the object. In general, such masks are not desirable because of the need to manually position them, thus leading to increased acquisition times. Fortunately, many methods to spatially modulate the THz beam have been demonstrated in the literature[26] especially in the context of single-pixel imaging and compressive sensing. For example, mounting the metallic masks on a spinning disk would ensure a rapid mask shuffling.[27] To forego completely the use of moving components, one can spatially modulate the THz beam in amplitude and/or in phase using active metamaterials,[28,29] micromirror arrays[30] or liquid crystals.[31−33] In addition to allowing rapid mask shuffling, these techniques allow the desired masks to be directly patterned in the incident beam, thus, forgoing the need to physically contact the object with the masks.

Another promising setup would be to place the object on a semiconductor substrate. Then, the different binary amplitude

https://dx.doi.org/10.1021/acsphotonics.0c00711
ACS Photonics 2020, 7, 1866−1875

masks could be optically pumped using a digital micromirror device.[13] Because the optical illumination is deeply subwavelength (compared to the THz wavelength) and by using very thin semiconductor wafers, very small pixels can be achieved. For example, a resolution of $\lambda/45$ at 0.75 THz was obtained using a compressed sensing approach.[23] Using the SODI technique, this resolution could be further improved.

Our proof of concept used a transmission geometry, while a reflection configuration is also possible for the SODI algorithm. Three-dimensional imaging can also be done using approaches similar to those used in visible SOFI.[17,34] In principle, the SODI algorithm can be used with near-field imaging systems[3] that use apertures[4] and tips.[5] However, in that case, because the obtained resolutions are already ultrasubwavelength (for example, 2 nm, $\lambda/150000$[5]), the masks that need to be used must also be ultrasubwavelength, which is hard to accomplish in practice.

Our algorithm can also be used with single-pixel detectors and compressive sensing. In single-pixel imaging, the image is obtained by successively measuring the object illuminated by a set of masks and reconstructed using an inverse matrix operation or a minimization approach.[2] To apply the SODI algorithm, one would need to first independently reconstruct N_t frames using the classical single-pixel imaging theory, and then use the SODI equation. This is interesting because subwavelength resolutions have already been demonstrated in THz compressed sensing (for example $\lambda/45$[23]) using an optically pumped semiconductor wafer as discussed above. The SODI algorithm could then be used in conjunction with single-pixel imaging and compressed sensing to increase the resolution further.

In the approaches discussed above, the image is constructed using a sequential set of measurements, either pixel-by-pixel in raster scans or mask-by-mask in single-pixel imaging, thus resulting in increased acquisition times. Interestingly, the SODI approach can be used with THz cameras that capture the full image in a parallel manner using array detectors.[19,20] Therefore, one could envision that the SODI algorithm could be used with THz microscopes using similar setups than those developed in the visible range. Borrowing ideas discussed above, the object could be deposited on a thin semiconductor substrate. Using optical pumping and a digital micromirror device, the different binary masks could be successively projected on the semiconductor. Of course, this would come at the expense of the framerate, because N_t frames are required to reconstruct a SODI image. However, using a photo-illuminated semiconductor substrate would give flexibility to rapidly change between a low-resolution high-framerate mode (without SODI) to a high-resolution low-framerate mode (with SODI).

CONCLUSION

In this paper, we detailed a novel Super-resolution Orthogonal Deterministic Imaging (SODI) technique and demonstrated its application in the THz spectral range. This computational imaging technique is inspired by the Super-resolution Optical Fluctuation Imaging (SOFI) that utilizes stochastic fluctuations in the intensity of the fluorophores integrated into the image under study. However, as there are no natural fluorophores in the THz spectral range, we substitute them by artificial blinkers in the form of judiciously and optimally constructed phase or binary amplitude mask sets. Starting from the equation of linear imaging systems, we find that it is possible to construct super-resolution images using highly transmissive (over 40% throughput) locally orthogonal mask sets. We experimentally demonstrated pure phase mask sets and binary amplitude mask sets resulting in a second order super-resolution reconstruction by processing only 8 images. We also showed how to extend the SODI algorithm to higher orders by using the concept of higher order mask orthogonality. We then numerically demonstrated solutions for the third and fourth order reconstructions using highly transmissive phase masks.

We believe that this work opens new possibilities in THz subwavelength imaging. Using the equation for linear imaging systems (eq 1), together with spatial modulation of the phase or amplitude of the THz wave, our methodology can already be applied in different imaging scenarios. For example, it can be directly translated to single-pixel imaging by modifying the photomodulated illumination masks.[12−14] Moreover, as we demonstrated experimentally, this technique can be used with incoherent measurements, which opens up new possibilities for subwavelength imaging using commercially available THz thermal cameras and THz field-effect transistor-based cameras. Finally, this work can be of interest to a larger optical community interested in other wavelengths, as it provides a clear theoretical framework for structuring illumination at a subwavelength scale using optimal phase and amplitude mask sets in order to improve image resolution beyond the diffraction limit.

ASSOCIATED CONTENT

Supporting Information

The Supporting Information is available free of charge at https://pubs.acs.org/doi/10.1021/acsphotonics.0c00711.

> Terahertz imaging system, fabrication of the object and the masks, determination of the size of the group of pixels in relation to the point spread function, reconstruction of the phase for binary amplitude masks, impact on the choice of the mesh and basis on the second-order SODI image reconstruction, and super-resolution reconstruction of order 4 (PDF)

AUTHOR INFORMATION

Corresponding Author

Maksim Skorobogatiy − *Engineering Physics, Polytechnique Montréal, Montréal, Canada*; Email: maksim.skorobogatiy@polymtl.ca

Authors

Hichem Guerboukha − *Engineering Physics, Polytechnique Montréal, Montréal, Canada*; orcid.org/0000-0002-7775-2011

Yang Cao − *Engineering Physics, Polytechnique Montréal, Montréal, Canada*

Kathirvel Nallappan − *Engineering Physics and Electrical Engineering, Polytechnique Montréal, Montréal, Canada*

Complete contact information is available at: https://pubs.acs.org/10.1021/acsphotonics.0c00711

Funding

This work was supported by the Canada Research Chair 1 of Prof. Skorobogatiy in Ubiquitous THz photonics and Canada Foundation for Innovation (CFI). H.G. acknowledges the support of the Natural Sciences and Engineering Research

Council of Canada (NSERC) and the Fonds de Recherche du Québec − Nature et Technologies (FRQNT).

Notes

The authors declare no competing financial interest.

REFERENCES

(1) Dhillon, S. S.; Vitiello, M. S.; Linfield, E. H.; Davies, A. G.; Hoffmann, M. C.; Booske, J.; Paoloni, C.; Gensch, M.; Weightman, P.; Williams, G. P.; Castro-Camus, E.; Cumming, D. R. S.; Simoens, F.; Escorcia-Carranza, I.; Grant, J.; Lucyszyn, S.; Kuwata-Gonokami, M.; Konishi, K.; Koch, M.; Schmuttenmaer, C. A.; Cocker, T. L.; Huber, R.; Markelz, A. G.; Taylor, Z. D.; Wallace, V. P.; Zeitler, J. A.; Sibik, J.; Korter, T. M.; Ellison, B.; Rea, S.; Goldsmith, P.; Cooper, K. B.; Appleby, R.; Pardo, D.; Huggard, P. G.; Krozer, V.; Shams, H.; Fice, M.; Renaud, C.; Seeds, A.; Stöhr, A.; Naftaly, M.; Ridler, N.; Clarke, R.; Cunningham, J. E.; Johnston, M. B. The 2017 terahertz science and technology roadmap. *J. Phys. D: Appl. Phys.* **2017**, *50* (4), 043001.

(2) Guerboukha, H.; Nallappan, K.; Skorobogatiy, M. Toward real-time terahertz imaging,. *Adv. Opt. Photonics* **2018**, *10* (4), 843−938.

(3) Adam, A. J. L. L. Review of near-field terahertz measurement methods and their applications: how to achieve sub-wavelength resolution at THz frequencies,. *J. Infrared, Millimeter, Terahertz Waves* **2011**, *32* (8−9), 976−1019.

(4) Mitrofanov, O.; Brener, I.; Luk, T. S.; Reno, J. L. Photoconductive terahertz near-field detector with a hybrid nanoantenna array cavity. *ACS Photonics* **2015**, *2* (12), 1763−1768.

(5) Cocker, T. L.; Jelic, V.; Gupta, M.; Molesky, S. J.; Burgess, J. A. J.; Reyes, G. D. L.; Titova, L. V.; Tsui, Y. Y.; Freeman, M. R.; Hegmann, F. A. An ultrafast terahertz scanning tunneling microscope. *Nat. Photonics* **2013**, *7* (8), 620.

(6) Chernomyrdin, N. V.; Kucheryavenko, A. S.; Kolontaeva, G. S.; Katyba, G. M.; Dolganova, I. N.; Karalkin, P. A.; Ponomarev, D. S.; Kurlov, V. N.; Reshetov, I. V.; Skorobogatiy, M.; Tuchin, V. V.; Zaytsev, K. I. Reflection-mode continuous-wave 0.15 λ-resolution terahertz solid immersion microscopy of soft biological tissues. *Appl. Phys. Lett.* **2018**, *113* (11), 111102.

(7) Pham, H. H. N.; Hisatake, S.; Minin, O. V.; Nagatsuma, T.; Minin, I. V. Enhancement of spatial resolution of terahertz imaging systems based on terajet generation by dielectric cube. *APL Photonics* **2017**, *2* (5), 056106.

(8) Blanchard, F.; Doi, A.; Tanaka, T.; Hirori, H.; Tanaka, H.; Kadoya, Y.; Tanaka, K. Real-time terahertz near-field microscope. *Opt. Express* **2011**, *19* (9), 8277−8284.

(9) Amirkhan, F.; Sakata, R.; Takiguchi, K.; Arikawa, T.; Ozaki, T.; Tanaka, K.; Blanchard, F. Characterization of thin-film optical properties by THz near-field imaging method. *J. Opt. Soc. Am. B* **2019**, *36* (9), 2593−2601.

(10) Grzyb, J.; Heinemann, B.; Pfeiffer, U. R. Solid-state terahertz superresolution imaging device in 130-nm SiGe BiCMOS technology. *IEEE Trans. Microwave Theory Tech.* **2017**, *65* (11), 4357−4372.

(11) Chan, W. L.; Charan, K.; Takhar, D.; Kelly, K. F.; Baraniuk, R. G.; Mittleman, D. M. A single-pixel terahertz imaging system based on compressed sensing. *Appl. Phys. Lett.* **2008**, *93* (12), 121105.

(12) Shrekenhamer, D.; Watts, C. M.; Padilla, W. J. Terahertz single pixel imaging with an optically controlled dynamic spatial light modulator. *Opt. Express* **2013**, *21* (12), 12507−12518.

(13) Stantchev, R. I.; Sun, B.; Hornett, S. M.; Hobson, P. A.; Gibson, G. M.; Padgett, M. J.; Hendry, E. Noninvasinve, near-field terahertz imaging of hidden objects using a single-pixel detector. *Science Advances* **2016**, *2* (6), No. e1600190.

(14) Zhao, J.; E, Y.; Williams, K.; Zhang, X.-C.; Boyd, R. W. Spatial sampling of terahertz fields with sub-wavelength accuracy via probe-beam encoding. *Light: Sci. Appl.* **2019**, *8* (1), 55.

(15) Godin, A. G.; Lounis, B.; Cognet, L. Super-resolution microscopy approaches for live cell imaging. *Biophys. J.* **2014**, *107* (8), 1777−1784.

(16) Wöll, D.; Flors, C. Super-resolution fluorescence imaging for materials science. *Small Methods* **2017**, *1* (10), 1700191.

(17) Dertinger, T.; Colyer, R.; Iyer, G.; Weiss, S.; Enderlein, J. Fast, background-free, 3D super-resolution optical fluctuation imaging (SOFI). *Proc. Natl. Acad. Sci. U. S. A.* **2009**, *106* (52), 22287−22292.

(18) Dertinger, T.; Colyer, R.; Vogel, R.; Enderlein, J.; Weiss, S. Achieving increased resolution and more pixels with superresolution optical fluctuation imaging (SOFI). *Opt. Express* **2010**, *18* (18), 18875−18885.

(19) Simoens, F.; Meilhan, J. Terahertz real-time imaging uncooled array based on antenna- and cavity-coupled bolometers. *Philos. Trans. R. Soc., A* **2014**, *372* (2012), 20130111.

(20) Zdanevicius, J.; Bauer, M.; Boppel, S.; Palenskis, V.; Lisauskas, A.; Krozer, V.; Roskos, H. G. Camera for high-speed THz imaging. *J. Infrared, Millimeter, Terahertz Waves* **2015**, *36* (10), 986−997.

(21) Wade, C. G.; Sibalic, N.; de Melo, N. R.; Kondo, J. M.; Adams, C. S.; Weatherill, K. J. Real-time near-field terahertz imaging with atomic optical fluorescence. *Nat. Photonics* **2017**, *11* (1), 40.

(22) Phillips, D. B.; Sun, M.-J.; Taylor, J. M.; Edgar, M. P.; Barnett, S. M.; Gibson, G. M.; Padgett, M. J. Adaptive foveated single-pixel imaging with dynamic supersampling. *Science Advances* **2017**, *3* (4), No. e1601782.

(23) Stantchev, R. I.; Phillips, D. B.; Hobson, P.; Hornett, S. M.; Padgett, M. J.; Hendry, E. Compressed sensing with near-field THz radiation. *Optica* **2017**, *4* (8), 989−992.

(24) Bethe, H. A. Theory of diffraction by small holes. *Phys. Rev.* **1944**, *66* (7−8), 163−182.

(25) Bouwkamp, C. J. On the diffraction of electromagnetic waves by small circular disks and holes. *Philips Research Reports* **1950**, *5*, 401−422.

(26) Rahm, M.; Li, J.-S.; Padilla, W. THz wave modulators: a brief review on different modulation techniques. *Journal of Infrared, Millimeter, and Terahertz Waves* **2013**, *31*, 1−27.

(27) Shen, H.; Gan, L.; Newman, N.; Dong, Y.; Li, C.; Huang, Y.; Shen, Y. C. Spinning disk for compressive imaging. *Opt. Lett.* **2012**, *37* (1), 46−48.

(28) Rout, S.; Sonkusale, S. R. A low-voltage high-speed terahertz spatial light modulator using active metamaterial. *APL Photonics* **2016**, *1* (8), 086102.

(29) Watts, C. M.; Shrekenhamer, D.; Montoya, J.; Lipworth, G.; Hunt, J.; Sleasman, T.; Krishna, S.; Smith, D. R.; Padilla, W. J. Terahertz compressive imaging with metamaterial spatial light modulators. *Nat. Photonics* **2014**, *8*, 605−609.

(30) Kappa, J.; Sokoluk, D.; Klingel, S.; Shemelya, C.; Oesterschulze, E.; Rahm, M. Electrically reconfigurable micromirror array for direct spatial light modulation of terahertz waves over a bandwidth wider than 1 THz,. *Scientific Reports* **2019**, *9*, 2597.

(31) Yang, J.; Xia, T.; Jing, S.; Deng, G.; Lu, H.; Fang, Y.; Yin, Z. Electrically tunable reflective terahertz phase shifter based on liquid crystal. *J. Infrared, Millimeter, Terahertz Waves* **2018**, *39*, 439−446.

(32) Du, Y.; Tian, H.; Cui, X.; Wang, H.; Zhou, Z.-X. Electrically tunable liquid crystal terahertz phase shifter driven by transparent polymer electrodes. *Journal of Materials Chemistry C* **2016**, *19*, 4138−4142.

(33) Wang, L.; Ge, S.; Hu, W.; Nakajima, M.; Lu, Y. Tunable reflective liquid crystal terahertz waveplates. *Opt. Mater. Express* **2017**, *7* (6), 2023−2029.

(34) Geissbuehler, S.; Sharipov, A.; Godinat, A.; Bocchio, N. L.; Sandoz, P. A.; Huss, A.; Jensen, N. A.; Jakobs, S.; Enderlein, J.; Goot, F. G.; Dubikovskaya, E. A.; Lasser, T.; Leutenegger, M. Live-cell multiplane three-dimensional super-resolution optical fluctuation imaging. *Nat. Commun.* **2014**, *5*, 5830.

https://dx.doi.org/10.1021/acsphotonics.0c00711
ACS Photonics 2020, 7, 1866−1875